ACS APPLIED MATERIALS & INTERFACES

www.acsami.org

Research Article

Engineering the Interfacial Microenvironment via Surface Hydroxylation to Realize the Global Optimization of Electrochemical CO_2 Reduction

Xu Han,[○] Ting Zhang,[○] Martí Biset-Peiró, Xuan Zhang, Jian Li,* Weiqiang Tang,* Pengyi Tang, Joan Ramon Morante, and Jordi Arbiol*

Cite This: *ACS Appl. Mater. Interfaces* 2022, 14, 32157−32165

Read Online

ACCESS | Metrics & More | Article Recommendations | Supporting Information

ABSTRACT: The adsorption and activation of CO_2 on the electrode interface is a prerequisite and key step for electrocatalytic CO_2 reduction reaction (eCO_2 RR). Regulating the interfacial microenvironment to promote the adsorption and activation of CO_2 is thus of great significance to optimize overall conversion efficiency. Herein, a CO_2-philic hydroxyl coordinated ZnO (ZnO−OH) catalyst is fabricated, for the first time, via a facile MOF-assisted method. In comparison to the commercial ZnO, the as-prepared ZnO−OH exhibits much higher selectivity toward CO at lower applied potential, reaching a Faradaic efficiency of 85% at −0.95 V versus RHE. To the best of our knowledge, such selectivity is one of the best records in ZnO-based catalysts reported till date. Density functional theory calculations reveal that the coordinated surficial −OH groups are not only favorable to interact with CO_2 molecules but also function in synergy to decrease the energy barrier of the rate-determining step and maintain a higher charge density of potential active sites as well as inhibit undesired hydrogen evolution reaction. Our results indicate that engineering the interfacial microenvironment through the introduction of CO_2-philic groups is a promising way to achieve the global optimization of eCO_2 RR via promoting adsorption and activation of CO_2.

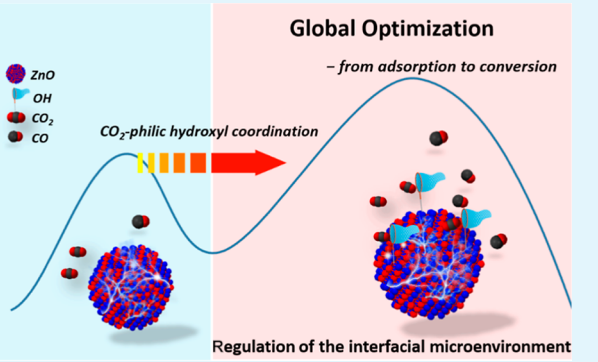

KEYWORDS: *ZnO, surficial hydroxyls, CO_2 adsorption, CO_2 activation, metal−organic frameworks (MOFs)*

1. INTRODUCTION

The electrochemical CO_2 reduction reaction (eCO_2 RR) into various fuels and value-added chemicals is a promising method to eliminate excessive greenhouse gas and realize energy reuse toward carbon recycling.[1−4] Considering the products of eCO_2 RR, carbon monoxide (CO), an important raw material for top-level organic chemical products, has high industrial value.[5−7] Theoretically, CO_2-to-CO conversion goes through the following steps: (1) adsorption of CO_2 and activation through a proton-coupled electron transfer process to generate COOH* intermediates; (2) the adsorbed COOH* intermediate is further reduced to form CO* and water; and (3) CO* is desorbed from the surface of the catalyst to form the CO product.[8−12] Due to the poor solubility of CO_2 in the aqueous electrolyte, the transformation of CO_2 from the gas feed to the surface of active sites is a minimum prerequisite for the follow-up steps of eCO_2 RR, thus limiting the overall conversion efficiency.[13,14]

Zinc oxide (ZnO), characterized by its huge reserves and for being cost-friendly, has been widely investigated for generating CO with moderate selectivity.[15−21] The oxidation state of Zn in ZnO as a clear active site provides infinite possibilities to enhance the eCO_2 RR efficiency.[18−21] For example, an increased number of active sites could be induced by modulating the ZnO morphology to expose abundant edge facets;[17] the ratio of H_2/CO obtained on ZnO electrocatalysts could be tuned through controlling the defects and facets.[19] However, almost no attention has been paid to the interfacial microenvironment between ZnO catalysts and CO_2, a key factor to affect its adsorption and activation. Generally, the adsorption and activation of non-polar CO_2 occur only at the interface of the solid electrocatalyst with the liquid electrolyte and CO_2 molecules by weak interactions.[11,22−25]

Introducing carbon dioxide-philic functional groups, which have strong interaction with CO_2 molecules, is an appealing route to manipulate the interface to enhance CO_2 affinities.[11,26−30] It is also anticipated that the CO_2-philic

Received: May 23, 2022
Accepted: June 29, 2022
Published: July 11, 2022

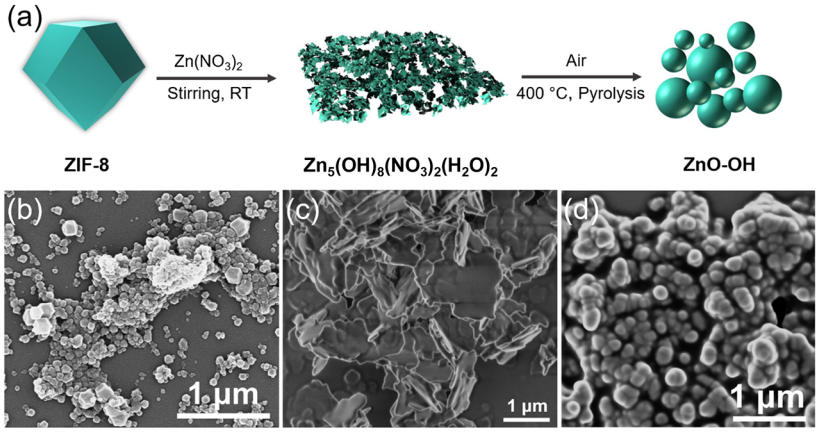

Figure 1. (a) Schematic illustration for the formation process of the ZnO−OH. SEM image of (b) ZIF-8, (c) $Zn_5(OH)_8(NO_3)_2(H_2O)_2$ and (d) ZnO−OH.

functional groups on the surface could modulate the electronic structure of the catalyst to further manipulate the formation of the sequent intermediates in the CO_2-to-CO conversion.[11,29] With this in mind, −OH groups, a kind of CO_2-philic functional groups, for the first time, were introduced on the surface of ZnO catalysts (ZnO−OH) via a simple ZIF-8-assisted (ZIF stands for zeolitic imidazolate frameworks) method. Compared to the commercial ZnO, the ZnO−OH exhibited much higher selectivity toward CO at a relatively lower applied potential and reached a FE_{CO} maximum of 85% at −0.95 V versus RHE, which is one of the best values among ZnO-based catalysts reported till date (see Table S4). Density functional theory (DFT) calculations indicated the existence of strong attraction between the ZnO−OH and the CO_2 molecule, which is beneficial to the adsorption of CO_2. Furthermore, the hydroxyl groups play an important role in facilitating the formation of the follow-up intermediates (COOH* and CO*), simultaneously limiting the undesired hydrogen evolution reaction (HER). All the results reveal the crucial role of CO_2-philic −OH groups in promoting the interfacial adsorption and activation of CO_2 to realize the global optimization of CO_2 electroreduction, which benefits the understanding of the relevant mechanism in eCO_2 RR and rational design of future high-efficient electrocatalysts.

2. EXPERIMENTAL SECTION

2.1. Chemicals. If not specified, all chemical reagents were obtained from Sigma-Aldrich and used directly. Zinc nitrate hexahydrate [$Zn(NO_3)_2{\cdot}6H_2O$], 2-methylimidazole (2-mim), commercial zinc oxide (ZnO), ethanol, and sodium bicarbonate ($NaHCO_3$) were all of analytical grade. The Nafion membrane (N-117, 0.18 mm thick) and carbon paper were obtained from Alfa Aesar.

2.2. Material Preparation. *2.2.1. Preparation of ZIF-8.* The fabrication process of ZIF-8 is similar to the process reported in the literature.[31] 50 mL of methanol aqueous solution containing 2-mim (1.230 g) was added into the methanol aqueous solution of $Zn(NO_3)_2{\cdot}6H_2O$ (50 mL, 1.115 g) with magnetic stirring to form homogeneous solution. After 24 h reaction without stirring at room temperature, the white solid was then taken out, washed by methanol several times, and vacuum dried overnight.

2.2.2. Preparation of $Zn_5(OH)_8(NO_3)_2(H_2O)_2$. 100 mg of ZIF-8 was etched by immersing into an ethanol solution (100 mL) containing 0.5 g of $Zn(NO_3)_2{\cdot}6H_2O$ with stirring for 30 min. The obtained $Zn_5(OH)_8(NO_3)_2(H_2O)_2$ sample was then taken out, washed with ethanol, and dried in vacuum oven overnight.

2.2.3. Preparation of ZnO−OH. The as-prepared $Zn_5(OH)_8(NO_3)_2(H_2O)_2$ powders were put at the porcelain boat. Subsequently, the samples were placed in a tube furnace and heated at 400 °C in air for 90 min to yield ZnO−OH (10 °C/min). Similarly, L-ZnO-OH and H−ZnO−OH were prepared by pyrolysis of $Zn_5(OH)_8(NO_3)_2(H_2O)_2$ that were treated by 0.4 or 0.6 g $Zn(NO_3)_2{\cdot}6H_2O$, respectively.

2.2.4. Preparation of D−ZnO. The as-prepared ZIF-8 powders were put at the porcelain boat with a direct pyrolysis at 400 °C for 90 min to yield D−ZnO.

2.3. Ink Preparation. 5 mg of the powder sample and 100 μL of Nafion solutions (5 wt %) were dissolved in 1 mL of ethanol under ultrasonication to form a homogeneous solution. 500 μL of the above inks were dropped onto the surface of the carbon paper (1 × 1 cm^2). The loading mass of the catalyst was determined as ∼3 mg/cm^2.

2.4. Electrochemical Characterization. The electrocatalytic performance was characterized in a three-electrode H-type cell system with two-compartments separated by a Nafion N-117 membrane, including a reference electrode (Ag/AgCl electrode), a counter electrode (Pt plate), and a working electrode (catalyst-loaded carbon paper). All potentials were referred to the RHE with $E_{RHE} = E^0_{Ag/AgCl} + E_{Ag/AgCl} + 0.059 \times pH$.[32,33] A BioLogic VMP3 electrochemical workstation was used to perform electrochemical experiments.

During electrochemical CO_2 reduction experiments, the CO_2 gas was delivered with a rate of 20 mL min^{-1} into the cell, and gas chromatography was used to test the final gas phase composition every 20 min. Meanwhile, we collected data three times to get an average value.

3. RESULTS AND DISCUSSION

3.1. Characterization of the Sample. In order to understand the influence of the −OH group on the CO_2 adsorption, DFT was first used to calculate the free energy of CO_2 adsorption on two representative models for ZnO and ZnO−OH (Figure S1). Compared to the negligible adsorption Gibbs free energy of CO_2 molecule on the pristine ZnO (−0.0028 eV), a much larger adsorption energy of −0.1466 eV was observed on ZnO−OH, revealing that the CO_2 adsorption on the ZnO−OH is more feasible. The increase in the CO_2 adsorption affinity is beneficial for the following eCO_2 RR and, in parallel, inhibits the reduction of protons (hydrogen evolution) in the electrolyte.[26,29]

With the guidance of above DFT calculations, ZnO with rich surficial −OH was synthesized via a novel MOF-assisted procedure (Figure 1a). In brief, ZIF-8 as a precursor was first transformed into a hydroxide intermediate by virtue of adding a given amount of $Zn(NO_3)_2$ solution at room temperature. Afterward, the ZnO with rich surficial −OH (ZnO−OH) was obtained through pyrolysis of the above hydroxide inter-

https://doi.org/10.1021/acsami.2c09129
ACS Appl. Mater. Interfaces 2022, 14, 32157−32165

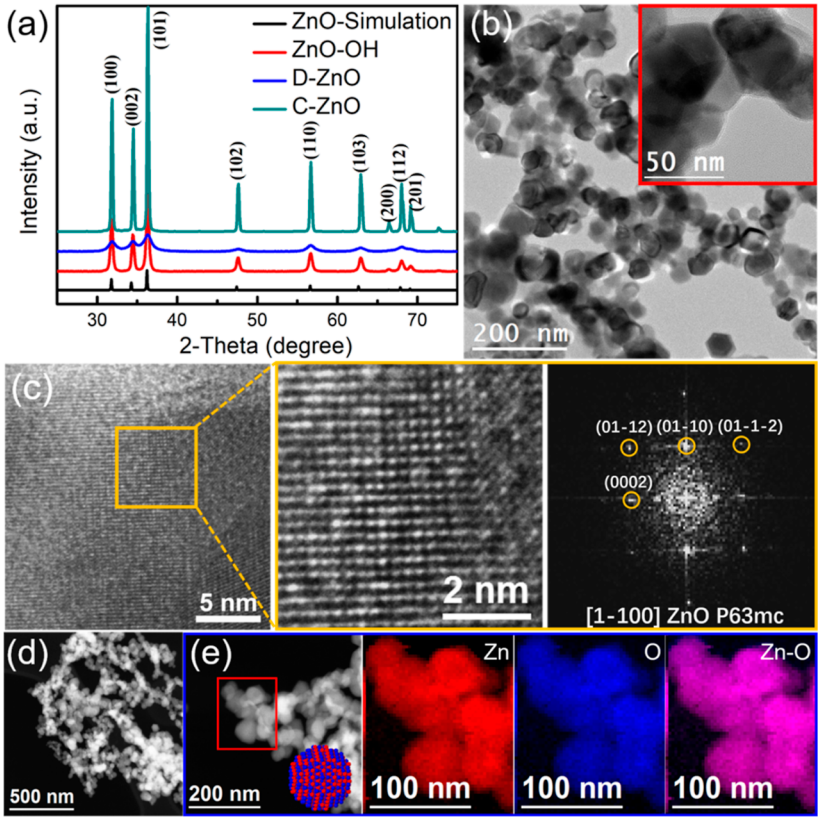

Figure 2. (a) XRD patterns. (b) Bright field TEM images showing the morphology of the ZnO−OH sample. The inset corresponds to a magnified detail of the studied area; (c) HRTEM image (left) and corresponding magnified detail (middle) with the corresponding indexed fast Fourier transform spectrum (right); (d) high-angle annular dark field scanning transmission electron microscopy (HAADF STEM) image; (e) HAADF STEM image and representative EELS chemical composition maps obtained from the red squared area in the STEM micrograph. Individual maps obtained from the Zn $L_{2,3}$-edges at 1020 eV (red), O K-edges at 532 eV (blue), and Zn−O composite map. Inset in (e) shows a 3D atomic supercell model of a ZnO nanoparticle (Zn and O atoms are represented in red and blue, respectively).

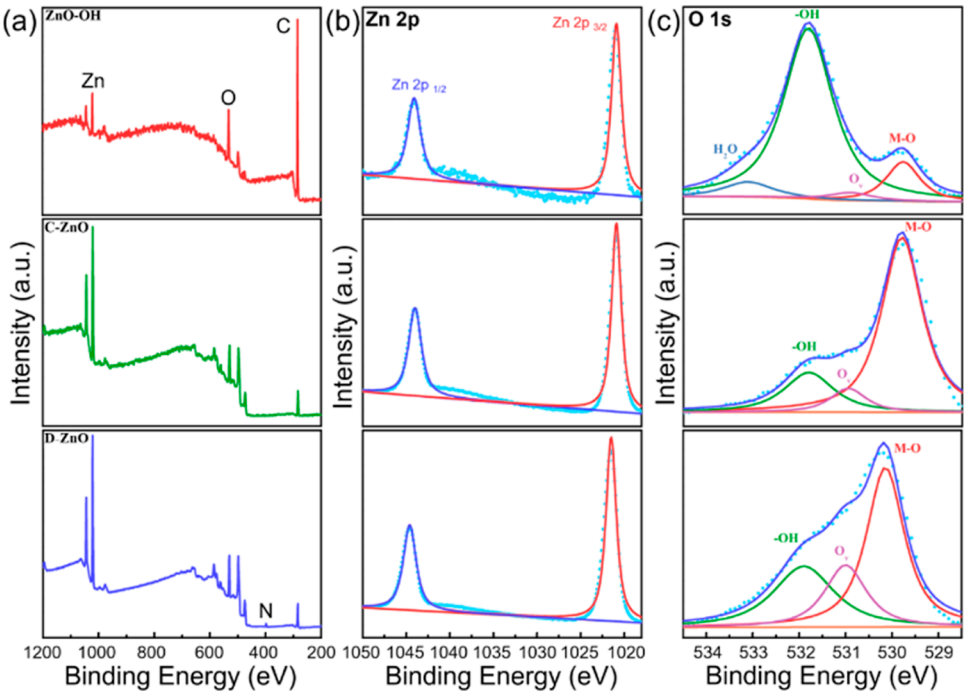

Figure 3. (a) XPS survey spectra and (b) high-resolution XPS spectra of Zn 2p and (c) O 1s for ZnO−OH (top), C−ZnO (middle), and D−ZnO (bottom).

https://doi.org/10.1021/acsami.2c09129
ACS Appl. Mater. Interfaces 2022, 14, 32157−32165

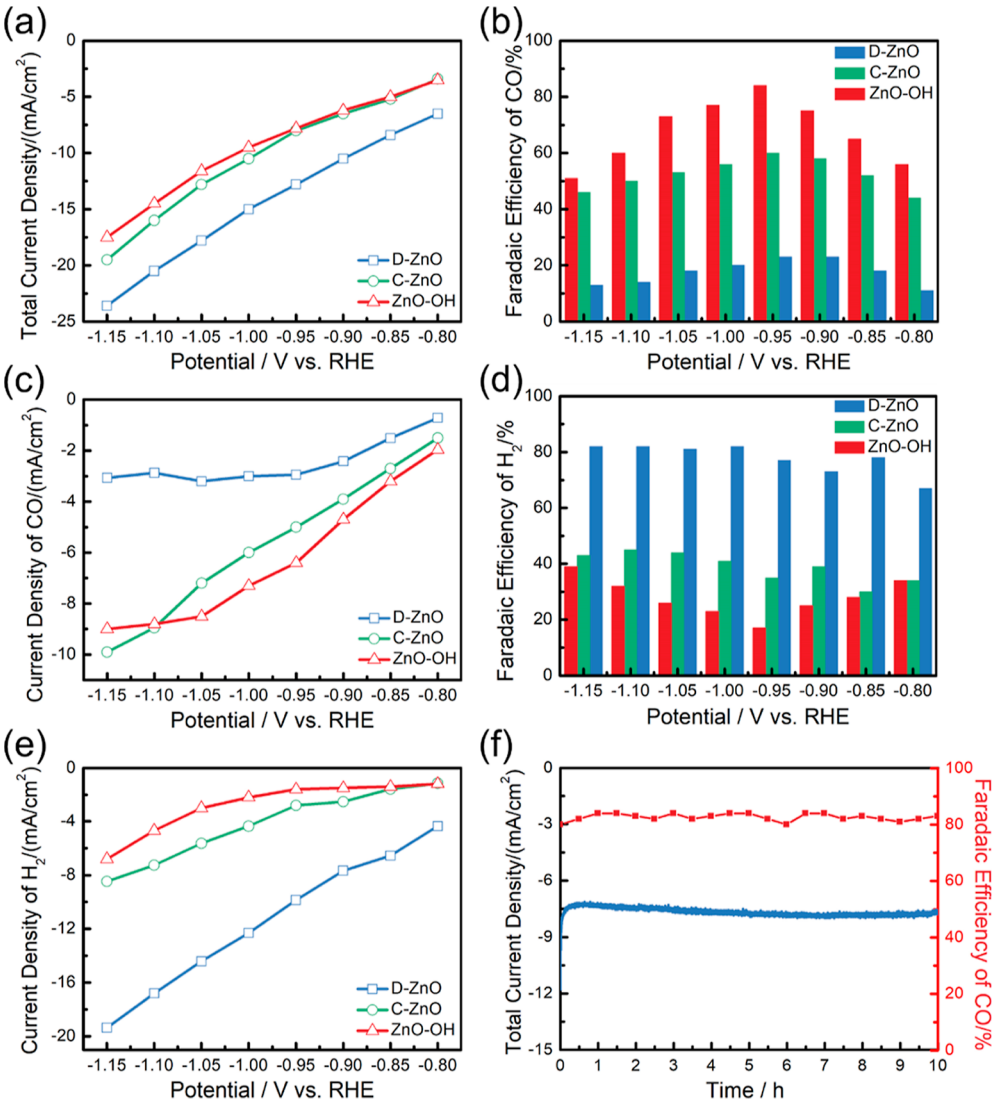

Figure 4. Electrocatalytic performance tests for ZnO−OH, D−ZnO and C−ZnO. (a) Total current density at various potentials. (b) FE of CO. (c) Current density of CO and (d) FE of H_2. (e) Current density of H_2 on ZnO−OH, D−ZnO, and C−ZnO. (f) Stability test for the ZnO−OH catalyst at −0.95 V vs RHE.

mediate under air. The high crystallinity of the as-prepared ZIF-8 and the corresponding hydroxide intermediate were first confirmed by powder X-ray diffraction (XRD) measurements. The ZIF-8 samples exhibited similar crystal patterns as expected for the standard ZIF-8 structure (Figure S2a).[31,34] In the case of the hydroxide intermediate sample, new diffraction peaks belonging to the $Zn_5(OH)_8(NO_3)_2(H_2O)_2$ phase appeared, indicating that the treatment changed the crystal structure of the pristine ZIF-8 (Figure S2b).[35,36] Field emission scanning electron microscopy revealed that sheet-shaped nanostructures were formed for the $Zn_5(OH)_8(NO_3)_2(H_2O)_2$ sample, different from the characteristic rhombic dodecahedral morphology of the ZIF-8 sample (Figures 1b,c and S3). Elemental composition maps indicated the existence of an additional O signal in the $Zn_5(OH)_8(NO_3)_2(H_2O)_2$ sample (Figures S4 and S5), while high-resolution TEM (HRTEM) analyses (Figure S6) further proved that ZIF-8 successfully transformed into the $Zn_5(OH)_8(NO_3)_2(H_2O)_2$ structure.

In order to clarify the uniqueness of the ZnO−OH obtained by our method, a reference D−ZnO sample was synthesized through direct pyrolysis under air of an as-prepared ZIF-8 sample without $Zn(NO_3)_2$ treatment. Meanwhile, commercial ZnO was also used as a reference sample and was labeled as C−ZnO. As shown in Figure 2a, all samples clearly showed a similar diffraction pattern with that of simulated ZnO, indicating the successful synthesis of the ZnO skeleton.[18,19] To investigate the morphology and phase evolution processes, SEM and TEM images of the three ZnO-based samples were obtained (Figures 1d, 2 and S7−10). The as-prepared ZnO−OH and the corresponding ZnO-based samples exhibited similar quasi-spherical shapes with irregular sizes. HRTEM analyses showed that all the ZnO-based samples displayed the typical hexagonal wurtzite ZnO phase (space group = $P6_3/mmc$) with $a = b = 3.2900$ Å and $c = 5.3000$ Å.[37−40] Electron energy loss spectroscopy (EELS) demonstrated the uniform distributions of Zn and O throughout all samples.

X-ray photoelectron spectroscopy (XPS) was used to characterize the chemical valence state and surface compositions of the different catalysts. Figure 3a shows the presence of C, O, and Zn elements in all samples. The Zn 2p XPS core level spectra for all samples can be deconvoluted into two

https://doi.org/10.1021/acsami.2c09129
ACS Appl. Mater. Interfaces 2022, 14, 32157−32165

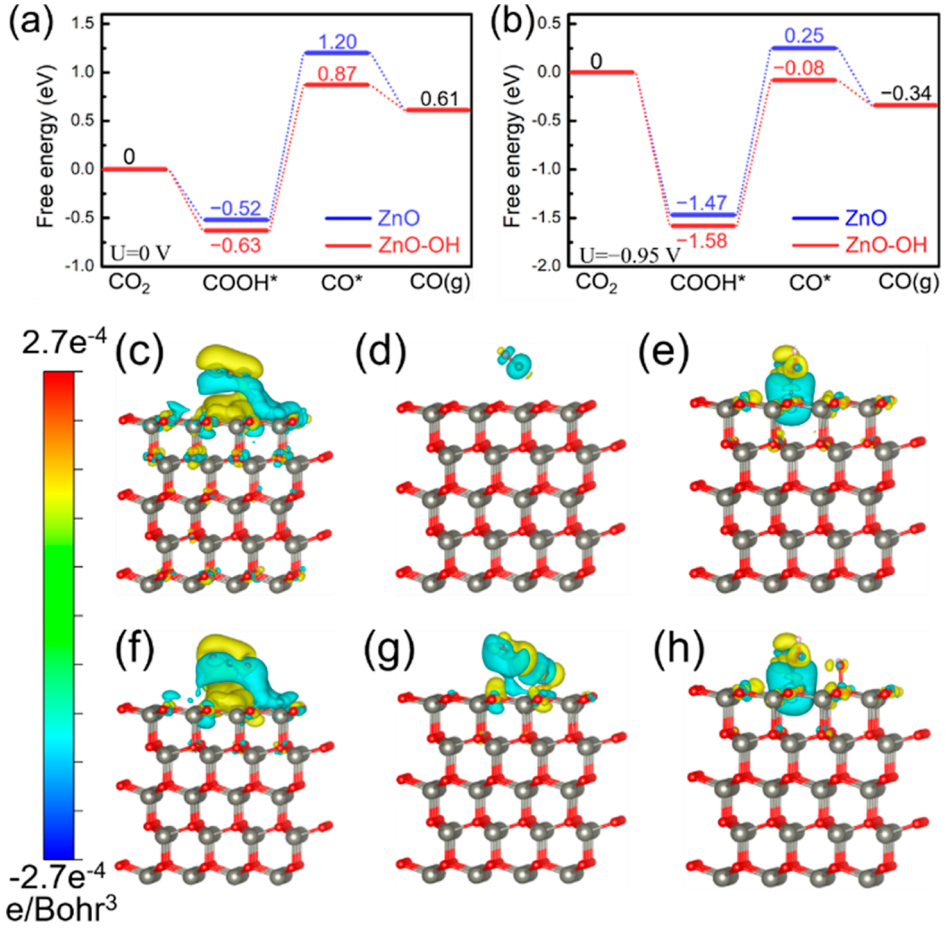

Figure 5. DFT studies of CO_2 RR. Free-energy profiles for the (a) CO_2 RR to CO at 0 and (b) −0.95 V (vs RHE) on the simulated models. Charge density difference for CO_2, CO, and *COOH adsorbed on a (c−e) ZnO slab and a (f−h) ZnO−OH slab. The gray, red, brown, and pink spheres represent Zn, O, C, and H atoms, respectively.

peaks, corresponding to Zn $2p_{3/2}$ and Zn $2p_{1/2}$ centered at around 1021 and 1044 eV, respectively, which indicates the presence of Zn^{2+} in all samples (Figure 3b).[19,31] The high-resolution XPS spectra obtained on the O 1s show three peaks in all three samples, corresponding to the typical metal−oxygen bond (Zn−O, 529.8 eV),[18,19] oxygen vacancy (O_v, 531.0 eV),[41] and −OH (531.7 eV),[42−44] respectively (Figure 3c). It is worth noting that there is a significant signal enhancement of the corresponding −OH peak obtained on the ZnO−OH sample in comparison to the C−ZnO and D−ZnO, which is ascribed to the higher density of surficial −OH groups. The integral-area ratios of the peak of surficial −OH groups to the peak of oxygen vacancy were calculated to be 51.3, 2.1, and 1.3 for ZnO−OH, C−ZnO, and D−ZnO. In comparison to C−ZnO, the much stronger FTIR peaks at around 1500 and 3400 cm^{-1} for ZnO−OH (Figure S11), which are attributed to the O−H stretch mode,[45] further confirmed the existence of large amount of −OH groups on the surface of ZnO−OH. All these observations demonstrated that the prepared ZnO−OH maintained the basic skeleton of ZnO with large amount of −OH groups on the surface. CO_2 adsorption measurements on different samples were further performed to support the strong interaction between −OH groups and CO_2 experimentally (Figure S12). The higher CO_2 uptake is observed on ZnO−OH sample, with the order following ZnO−OH (15.44 m^2/g) > D−ZnO (5.93 m^2/g) > C−ZnO (1.64 m^2/g). Such results demonstrated that the surface −OH groups of ZnO−OH promoted CO_2 adsorption remarkably, consistent with the DFT results (Figure S1).

3.2. eCO_2 RR Performance. Next, electrochemical CO_2 RR performances of the different samples were evaluated in 0.5 M $NaHCO_3$. All electrodes were pre-treated in an Ar-saturated electrolyte at −0.70 V versus RHE for 30 min to reach a stable current (Figure S13). The eCO_2 RR performance on the ZnO−OH sample was first evaluated by linear sweep voltammetry in both Ar- and CO_2-saturated electrolytes (Figure S14). A large increase in the current density observed on the ZnO−OH sample after replacement of an Ar atmosphere by CO_2 suggested that CO_2 was electrochemically reduced by the ZnO−OH sample.[46,47] Meanwhile, no obvious redox peaks were observed in the CO_2-saturated aqueous solution, which displayed that ZnO−OH tended to react with CO_2 molecules instead of suffering from self-reduction.[26] Figure 4a summarizes the measured total current density for ZnO−OH, D−ZnO, and C−ZnO samples. Although ZnO−OH and C−ZnO showed similar total reduction current densities, ZnO−OH showed the highest selectivity toward CO in a potential range from −0.80 to −1.15 V versus RHE, reaching the maximum Faradaic efficiency (FE) (CO) (85%) at −0.95 V versus RHE (Figure 4b). To the best of our knowledge, such high selectivity for CO at a low applied potential is the best record in ZnO-based catalysts reported so far (Table S4). The largest potential-dependent CO partial current densities observed on ZnO−OH further demonstrated

https://doi.org/10.1021/acsami.2c09129
ACS Appl. Mater. Interfaces 2022, 14, 32157−32165

the excellent activity and selectivity toward CO (Figure 4c). A decreasing trend in FE (CO) for ZnO−OH and C−ZnO was observed when the potential shifted to more negative values, which mainly stems from the dominance of the H_2 generation over the eCO_2 RR (Figure 4d). This assumption was further confirmed by the potential-dependent H_2 current densities for the different catalysts (Figure 4e). The intrinsic activity of the catalysts was disclosed by the electrochemical active surface area (ECSA).[32] As shown in Figure S15, the C_{dl} of ZnO−OH, D−ZnO, and C−ZnO samples was 0.05, 0.07, and 0.02 μF cm^{-2}, respectively, which indicated that the ECSA is not responsible for the activity of ZnO−OH. A similar phenomenon could be observed on the nitrogen adsorption−desorption isotherms and BET surface area (Figure S16). It is well known that those electrocatalysts with high specific surface area should endow the efficient exposure of electrocatalytic active sites, fast electrolyte penetration/diffusion, and free diffusion of intermediates.[48,49] In our case, the specific surface area of the ZnO−OH was much lower than that of D−ZnO, which suggests that the intrinsic catalytic activity of ZnO−OH sample arise from the presence of surficial −OH groups instead of the specific surface area.

To investigate the reaction kinetics on ZnO−OH during eCO_2 RR, Tafel slopes derived from the static state current densities for CO were calculated. The C−ZnO samples exhibit a Tafel slope of 36 mV dec^{-1}, close to 39 mV dec^{-1}, indicating that the rate-determining step (RDS) of CO_2 RR on C−ZnO powder corresponds to the initial proton-coupled electron transfer (Figure S17).[50] The much lower Tafel slopes (30 mV dec^{-1}) for the ZnO−OH catalyst indicated its remarkably improved kinetics toward CO conversion.[51−55] In addition, the effects of ZnO−OH samples treated by different amounts of $Zn(NO_3)_2$ on the CO_2 RR activity were also studied, which were denoted as L−ZnO−OH and H−ZnO−OH, respectively. Both the referential samples showed similar crystal patterns with simulated ZnO (Figure S18a) and morphology in comparison with spherical ZnO−OH (Figure S18b,c). However, the selectivity of L−ZnO−OH and H−ZnO−OH changed negatively (Figure S19), which is due to the decreased ratio between surficial −OH groups and oxygen vacancy (Figure S20).

To further investigate the stability of the ZnO−OH during the eCO_2 RR, a 10 h stability measurement was conducted. A current density of ca. −8.2 mA cm^{-2} and a FE(CO) over 80% were maintained during the 10 h test (Figure 4f). After the stability test, TEM analyses were performed to reveal the morphology and phase changes on the ZnO−OH sample, as shown in Figure S21. EELS compositional maps demonstrate that most of the ZnO−OH areas showed a uniform distribution of Zn and O. HRTEM analyses showed the presence of some metallic Zn nanoparticles with hexagonal phase (space group = $P6_3/mmc$). The presence of reduced Zn nanostructure can explain the slight efficiency loss after the stability test, evidencing the competition in the metal oxides between self-reduction and CO_2 reduction.[26,56]

3.3. DFT Calculations. The CO_2 RR process for the ZnO and ZnO−OH models was studied by DFT calculations to illustrate the origin of the improved CO_2 RR. The free-energy profiles at a potential of 0 V versus RHE for the three elementary steps and the two important intermediates (COOH* and CO*) in the CO_2 RR process are shown in Figure 5a. The ΔG for the formation of COOH* over commercial ZnO and the ZnO−OH catalysts is −0.52 and −0.63 eV, respectively. The stronger stabilization of surface COOH* on the ZnO−OH could increase the selectivity for the desired product CO. Besides, the following dissociation of COOH* assisted by the proton-electron transfer to produce CO* and H_2O is an endothermic and the RDS. To our excitement, ΔG increases by 1.72 and 1.5 eV on ZnO and ZnO−OH catalyst models, respectively, which means that the process of the CO* generation on the ZnO−OH slab is thermodynamically more favorable than that on the ZnO slab. As for the final step of CO desorption, the ΔG over the reference ZnO and the ZnO−OH catalyst is −0.59 and −0.26 eV, respectively. Such a relatively weak binding of CO* and above stronger stabilization of COOH* steer the electron and proton transfer to the formation of the CO product. Similar trends are also observed on the free-energy profiles at −0.95 V (vs RHE) (Figure 5b). The differential charge density for CO_2, CO, and COOH* on the ZnO−OH and ZnO slabs was also calculated and is shown in Figure 5c−h. The charge accumulation and deficit between them and the corresponding surface were presented with yellow and cyan iso-surfaces. Through contrastive analysis, the charge density difference of CO on the ZnO−OH slab was more prominent than that on the ZnO slab. To summarize, the ZnO−OH slab stabilizes the key intermediates via electronic interactions, which in synergy leads to an enhanced CO selectivity. More importantly, the Gibbs free energy for the CO_2 activation process on ZnO with two surficial −OH decreased by ca. 0.17 eV with respect to the ZnO with only one surficial −OH, which revealed that more surficial −OH coverage enhanced the adsorption of CO_2 (Figure S22). These calculated results were in good agreement with the experimental observations that the ZnO−OH sample exhibited better selectivity for CO_2 RR in comparison to the C−ZnO catalyst. Additionally, HER as a competing side reaction is also studied here (Figure S23). The stronger stability of H* on the surface could suppress HER effectively. It can be concluded that the HER is less active on ZnO−OH than that on the reference ZnO sample (−1.87 and −1.67 eV, respectively), suggesting that HER occurs more easily on ZnO without the surficial −OH coverage. Taken in all, the surface hydroxyls can not only facilitate the formation of COOH* and CO* via electronic interactions but also limit the undesired HER.

4. CONCLUSIONS

In summary, ZnO covered by surficial −OH groups was synthesized through a novel MOF-assisted method, which delicately optimize the interfacial microenvironment to promote the interfacial adsorption and activation of CO_2. The synthesized −OH-rich ZnO presents a FE_{CO} maximum of 85% at −0.95 V versus RHE, which is one of the best records among the state-of-the-art ZnO-based catalysts. DFT calculations confirmed that the surface −OH first boosts the adsorption of CO_2 at the interface and then promotes the generation of COOH* and CO* intermediates. Our findings revealed that tuning the interfacial microenvironment via the introduction of dioxide-philic functional groups is a promising way to achieve the global optimization via promotion of interfacial adsorption and activation of CO_2, which paves a new way to rationally design future highly active electrocatalysts for eCO_2 RR.

https://doi.org/10.1021/acsami.2c09129
ACS Appl. Mater. Interfaces 2022, 14, 32157−32165

■ ASSOCIATED CONTENT

Supporting Information

The Supporting Information is available free of charge at https://pubs.acs.org/doi/10.1021/acsami.2c09129.

Additional characterizations, DFT results, and electrocatalytic testing curves (PDF)

■ AUTHOR INFORMATION

Corresponding Authors

Jian Li − *Laboratory of Renewable Energy Science and Engineering, Institute of Mechanical Engineering EPFL, 1015 Lausanne, Switzerland*; Email: jian.li@epfl.ch

Weiqiang Tang − *State Key Laboratory of Chemical Engineering and School of Chemical Engineering, East China University of Science and Technology, 200237 Shanghai, China*; orcid.org/0000-0002-7726-4130; Email: wqtang@ecust.edu.cn

Jordi Arbiol − *Catalan Institute of Nanoscience and Nanotechnology (ICN2), CSIC and BIST, Barcelona 08193 Catalonia, Spain; ICREA, Barcelona 08010 Catalonia, Spain*; orcid.org/0000-0002-0695-1726; Email: arbiol@icrea.cat

Authors

Xu Han − *Catalan Institute of Nanoscience and Nanotechnology (ICN2), CSIC and BIST, Barcelona 08193 Catalonia, Spain*

Ting Zhang − *Catalan Institute of Nanoscience and Nanotechnology (ICN2), CSIC and BIST, Barcelona 08193 Catalonia, Spain; Catalonia Institute for Energy Research (IREC), Barcelona 08930 Catalonia, Spain*

Martí Biset-Peiró − *Catalonia Institute for Energy Research (IREC), Barcelona 08930 Catalonia, Spain*

Xuan Zhang − *Department of Materials Engineering, KU Leuven, 3001 Leuven, Belgium*

Pengyi Tang − *State Key Laboratory of Information Functional Materials, 2020 X-Lab, Shanghai Institute of Microsystem and Information Technology, Chinese Academy of Sciences, 200050 Shanghai, China*; orcid.org/0000-0002-2306-095X

Joan Ramon Morante − *Catalonia Institute for Energy Research (IREC), Barcelona 08930 Catalonia, Spain; Department of Physics, Universitat de Barcelona, Barcelona 08028 Catalonia, Spain*

Complete contact information is available at: https://pubs.acs.org/10.1021/acsami.2c09129

Author Contributions

○X.H. and T.Z. contributed equally to this paper.

Notes

The authors declare no competing financial interest.

■ ACKNOWLEDGMENTS

The authors acknowledge funding from Generalitat de Catalunya 2017 SGR 327 and 2017 SGR 1246. X.H., T.Z., J.R.M., and J.A. acknowledge funding from the projects (PID2020-116093RB-C42 and -C43), funded by MCIN/AEI/10.13039/501100011033/. ICN2 is supported by the Severo Ochoa program from Spanish MINECO (grant no. SEV-2017-0706). ICN2 and IREC are funded by the CERCA Programme/Generalitat de Catalunya. X.Z. acknowledges funding from FWO project (12ZV320N). Part of the present work has been performed in the framework of Universitat Autònoma de Barcelona Materials Science PhD program. X.H. thanks China Scholarship Council for scholarship support (201804910551).

■ REFERENCES

(1) Jin, S.; Hao, Z.; Zhang, K.; Yan, Z.; Chen, J. Advances and Challenges for the Electrochemical Reduction of CO_2 to CO: From Fundamentals to Industrialization. *Angew. Chem., Int. Ed.* **2021**, *60*, 20627−20648.

(2) Zhong, M.; Tran, K.; Min, Y.; Wang, C.; Wang, Z.; Dinh, C.-T.; De Luna, P.; Yu, Z.; Rasouli, A. S.; Brodersen, P.; Sun, S.; Voznyy, O.; Tan, C.-S.; Askerka, M.; Che, F.; Liu, M.; Seifitokaldani, A.; Pang, Y.; Lo, S.-C.; Ip, A.; Ulissi, Z.; Sargent, E. H. Accelerated Discovery of CO_2 Electrocatalysts Using Active Machine Learning. *Nature* **2020**, *581*, 178−183.

(3) Yang, B.; Liu, K.; Li, H.; Liu, C.; Fu, J.; Li, H.; Huang, J. E.; Ou, P.; Alkayyali, T.; Cai, C.; Duan, Y.; Liu, H.; An, P.; Zhang, N.; Li, W.; Qiu, X.; Jia, C.; Hu, J.; Chai, L.; Lin, Z.; Gao, Y.; Miyauchi, M.; Cortés, E.; Maier, S. A.; Liu, M. Accelerating CO_2 Electroreduction to Multicarbon Products via Synergistic Electric−Thermal Field on Copper Nanoneedles. *J. Am. Chem. Soc.* **2022**, *144*, 3039−3049.

(4) Li, H.; Zhou, H.; Zhou, Y.; Hu, J.; Miyauchi, M.; Fu, J.; Liu, M. Electric-Field Promoted C−C Coupling over Cu Nanoneedles for CO_2 Electroreduction to C2 Products. *Chin. J. Catal.* **2022**, *43*, 519−525.

(5) Guo, Q.; Liang, F.; Li, X.-B.; Gao, Y.-J.; Huang, M.-Y.; Wang, Y.; Xia, S.-G.; Gao, X.-Y.; Gan, Q.-C.; Lin, Z.-S.; Tung, C.-H.; Wu, L.-Z. Efficient and Selective CO_2 Reduction Integrated with Organic Synthesis by Solar Energy. *Chem* **2019**, *5*, 2605−2616.

(6) Yuan, X.; Wu, Y.; Jiang, B.; Wu, Z.; Tao, Z.; Lu, X.; Liu, J.; Qian, T.; Lin, H.; Zhang, Q. Interface Engineering of Silver-Based Heterostructures for CO_2 Reduction Reaction. *ACS Appl. Mater. Interfaces* **2020**, *12*, 56642−56649.

(7) Navarro, R. M.; Peña, M. A.; Fierro, J. L. G. Hydrogen Production Reactions from Carbon Feedstocks: Fossil Fuels and Biomass. *Chem. Rev.* **2007**, *107*, 3952−3991.

(8) Rosen, B. A.; Salehi-Khojin, A.; Thorson, M. R.; Zhu, W.; Whipple, D. T.; Kenis, P. J. A.; Masel, R. I. Ionic Liquid-Mediated Selective Conversion of CO_2 to CO at Low Overpotentials. *Science* **2011**, *334*, 643−644.

(9) Zhu, D. D.; Liu, J. L.; Qiao, S. Z. Recent Advances in Inorganic Heterogeneous Electrocatalysts for Reduction of Carbon Dioxide. *Adv. Mater.* **2016**, *28*, 3423−3452.

(10) Zhang, W.; Hu, Y.; Ma, L.; Zhu, G.; Wang, Y.; Xue, X.; Chen, R.; Yang, S.; Jin, Z. Progress and Perspective of Electrocatalytic CO_2 Reduction for Renewable Carbonaceous Fuels and Chemicals. *Adv. Sci.* **2018**, *5*, 1700275.

(11) Huang, Q.; Li, Q.; Liu, J.; Wang, Y. R.; Wang, R.; Dong, L. Z.; Xia, Y. H.; Wang, J. L.; Lan, Y.-Q. Disclosing CO_2 Activation Mechanism by Hydroxyl-Induced Crystalline Structure Transformation in Electrocatalytic Process. *Matter* **2019**, *1*, 1656−1668.

(12) Zhang, X.; Zhou, Y.; Zhang, H.; Li, H.; Liu, K.; Li, H.; Pan, H.; Hu, J.; Fu, J.; Chen, S.; Liu, M. Tuning the Electron Structure Enables the Nizn Alloy for CO_2 Electroreduction to Formate. *J. Energy Chem.* **2021**, *63*, 625−632.

(13) Xu, S.; Carter, E. A. Theoretical Insights into Heterogeneous (Photo)electrochemical CO_2 Reduction. *Chem. Rev.* **2019**, *119*, 6631−6669.

(14) Zhao, K.; Quan, X. Carbon-Based Materials for Electrochemical Reduction of CO_2 to C2+ Oxygenates: Recent Progress and Remaining Challenges. *ACS Catal.* **2021**, *11*, 2076−2097.

(15) Tan, D.; Lee, W.; Kim, Y. E.; Ko, Y. N.; Youn, M. H.; Jeon, Y. E.; Hong, J.; Jeong, S. K.; Park, K. T. SnO_2/ZnO Composite Hollow Nanofiber Electrocatalyst for Efficient CO_2 Reduction to Formate. *ACS Sustain. Chem. Eng.* **2020**, *8*, 10639−10645.

(16) Nguyen, D. L. T.; Jee, M. S.; Won, D. H.; Jung, H.; Oh, H.-S.; Min, B. K.; Hwang, Y. J. Selective CO_2 Reduction on Zinc

Electrocatalyst: The Effect of Zinc Oxidation State Induced by Pretreatment Environment. *ACS Sustain. Chem. Eng.* **2017**, *5*, 11377−11386.
(17) Xiang, Q.; Li, F.; Wang, J.; Chen, W.; Miao, Q.; Zhang, Q.; Tao, P.; Song, C.; Shang, W.; Zhu, H.; Deng, T.; Wu, J. Heterostructure of ZnO Nanosheets/Zn with a Highly Enhanced Edge Surface for Efficient CO_2 Electrochemical Reduction to CO. *ACS Appl. Mater. Interfaces* **2021**, *13*, 10837−10844.
(18) Geng, Z.; Kong, X.; Chen, W.; Su, H.; Liu, Y.; Cai, F.; Wang, G.; Zeng, J. Oxygen Vacancies in ZnO Nanosheets Enhance CO_2 Electrochemical Reduction to CO. *Angew. Chem., Int. Ed.* **2018**, *57*, 6054−6059.
(19) Daiyan, R.; Lovell, E. C.; Huang, B.; Zubair, M.; Leverett, J.; Zhang, Q.; Lim, S.; Horlyck, J.; Tang, J.; Lu, X.; Kalantar-Zadeh, K.; Hart, J. N.; Bedford, N. M.; Amal, R. Uncovering Atomic-Scale Stability and Reactivity in Engineered Zinc Oxide Electrocatalysts for Controllable Syngas Production. *Adv. Energy Mater.* **2020**, *10*, 2001381.
(20) Franco, F.; Rettenmaier, C.; Jeon, H. S.; Roldan Cuenya, B. Transition Metal-Based Catalysts for the Electrochemical CO_2 Reduction: From Atoms and Molecules to Nanostructured Materials. *Chem. Soc. Rev.* **2020**, *49*, 6884−6946.
(21) Liu, Y.; Yu, L.; Hu, Y.; Guo, C.; Zhang, F.; Lou, X. W. A Magnetically Separable Photocatalyst Based on Nest-Like γ-Fe_2O_3/ZnO Double-Shelled Hollow Structures with Enhanced Photocatalytic Activity. *Nanoscale* **2012**, *4*, 183−187.
(22) Resasco, J.; Chen, L. D.; Clark, E.; Tsai, C.; Hahn, C.; Jaramillo, T. F.; Chan, K.; Bell, A. T. Promoter Effects of Alkali Metal Cations on the Electrochemical Reduction of Carbon Dioxide. *J. Am. Chem. Soc.* **2017**, *139*, 11277−11287.
(23) Resasco, J.; Lum, Y.; Clark, E.; Zeledon, J. Z.; Bell, A. T. Effects of Anion Identity and Concentration on Electrochemical Reduction of CO_2. *ChemElectroChem* **2018**, *5*, 1064−1072.
(24) Liu, P.; Zheng, N. Coordination Chemistry of Atomically Dispersed Catalysts. *Natl. Sci. Rev.* **2018**, *5*, 636−638.
(25) Wang, Q.; Liu, K.; Fu, J.; Cai, C.; Li, H.; Long, Y.; Chen, S.; Liu, B.; Li, H.; Li, W.; Qiu, X.; Zhang, N.; Hu, J.; Pan, H.; Liu, M. Atomically Dispersed s-Block Magnesium Sites for Electroreduction of CO_2 to CO. *Angew. Chem., Int. Ed.* **2021**, *60*, 25241−25245.
(26) Deng, W.; Zhang, L.; Li, L.; Chen, S.; Hu, C.; Zhao, Z.-J.; Wang, T.; Gong, J. Crucial Role of Surface Hydroxyls on the Activity and Stability in Electrochemical CO_2 Reduction. *J. Am. Chem. Soc.* **2019**, *141*, 2911−2915.
(27) Yang, P.; Zhao, Z.-J.; Chang, X.; Mu, R.; Zha, S.; Zhang, G.; Gong, J. The Functionality of Surface Hydroxy Groups on the Selectivity and Activity of Carbon Dioxide Reduction over Cuprous Oxide in Aqueous Solutions. *Angew. Chem., Int. Ed.* **2018**, *57*, 7724−7728.
(28) Peng, Y.; Wang, L.; Luo, Q.; Cao, Y.; Dai, Y.; Li, Z.; Li, H.; Zheng, X.; Yan, W.; Yang, J.; Zeng, J. Molecular-Level Insight into How Hydroxyl Groups Boost Catalytic Activity in CO_2 Hydrogenation into Methanol. *Chem* **2018**, *4*, 613−625.
(29) Cui, C.; Han, J.; Zhu, X.; Liu, X.; Wang, H.; Mei, D.; Ge, Q. Promotional Effect of Surface Hydroxyls on Electrochemical Reduction of CO_2 over Sno_x/Sn Electrode. *J. Catal.* **2016**, *343*, 257−265.
(30) Yao, D.; Tang, C.; Vasileff, A.; Zhi, X.; Jiao, Y.; Qiao, S. Z. The Controllable Reconstruction of Bi-MOFs for Electrochemical CO_2 Reduction through Electrolyte and Potential Mediation. *Angew. Chem., Int. Ed.* **2021**, *60*, 18178−18184.
(31) Dou, S.; Song, J.; Xi, S.; Du, Y.; Wang, J.; Huang, Z. F.; Xu, Z. J.; Wang, X. Boosting Electrochemical CO_2 Reduction on Metal−Organic Frameworks via Ligand Doping. *Angew. Chem., Int. Ed.* **2019**, *58*, 4041−4045.
(32) Zhang, T.; Du, J.; Xi, P.; Xu, C. Hybrids of Cobalt/Iron Phosphides Derived from Bimetal−Organic Frameworks as Highly Efficient Electrocatalysts for Oxygen Evolution Reaction. *ACS Appl. Mater. Interfaces* **2017**, *9*, 362−370.
(33) Zhang, T.; Han, X.; Liu, H.; Biset-Peiró, M.; Li, J.; Zhang, X.; Tang, P.; Yang, B.; Zheng, L.; Morante, J. R.; Arbiol, J. Site-Specific Axial Oxygen Coordinated FeN_4 Active Sites for Highly Selective Electroreduction of Carbon Dioxide. *Adv. Funct. Mater.* **2022**, *32*, 2111446.
(34) Saliba, D.; Ammar, M.; Rammal, M.; Al-Ghoul, M.; Hmadeh, M. Crystal Growth of ZIF-8, ZIF-67, and Their Mixed-Metal Derivatives. *J. Am. Chem. Soc.* **2018**, *140*, 1812−1823.
(35) Schwenzer, B.; Pop, L. Z.; Neilson, J. R.; Sbardellati, T. B.; Morse, D. E. Nanostructured ZnS and CdS Films Synthesized Using Layered Double Hydroxide Films as Precursor and Template. *Inorg. Chem.* **2009**, *48*, 1542−1550.
(36) Shinagawa, T.; Watanabe, M.; Mori, T.; Tani, J.-i.; Chigane, M.; Izaki, M. Oriented Transformation from Layered Zinc Hydroxides to Nanoporous ZnO: A Comparative Study of Different Anion Types. *Inorg. Chem.* **2018**, *57*, 13137−13149.
(37) Utama, M. I. B.; Belarre, F. J.; Magen, C.; Peng, B.; Arbiol, J.; Xiong, Q. Incommensurate van der Waals Epitaxy of Nanowire Arrays: A Case Study with ZnO on Muscovite Mica Substrates. *Nano Lett.* **2012**, *12*, 2146−2152.
(38) de la Mata, M.; Magen, C.; Gazquez, J.; Utama, M. I. B.; Heiss, M.; Lopatin, S.; Furtmayr, F.; Fernández-Rojas, C. J.; Peng, B.; Morante, J. R.; Rurali, R.; Eickhoff, M.; Fontcuberta i Morral, A.; Xiong, Q.; Arbiol, J. Polarity Assignment in ZnTe, GaAs, ZnO, and GaN-AlN Nanowires from Direct Dumbbell Analysis. *Nano Lett.* **2012**, *12*, 2579−2586.
(39) de la Mata, M.; Zamani, R. R.; Martí-Sánchez, S.; Eickhoff, M.; Xiong, Q.; Fontcuberta i Morral, A.; Caroff, P.; Arbiol, J. The Role of Polarity in Nonplanar Semiconductor Nanostructures. *Nano Lett.* **2019**, *19*, 3396−3408.
(40) Li, J.; Slassi, A.; Han, X.; Cornil, D.; Ha-Thi, M. H.; Pino, T.; Debecker, D. P.; Colbeau-Justin, C.; Arbiol, J.; Cornil, J.; Ghazzal, M. N. Tuning the Electronic Bandgap of Graphdiyne by H-Substitution to Promote Interfacial Charge Carrier Separation for Enhanced Photocatalytic Hydrogen Production. *Adv. Funct. Mater.* **2021**, *31*, 2100994.
(41) Lei, F.; Sun, Y.; Liu, K.; Gao, S.; Liang, L.; Pan, B.; Xie, Y. Oxygen Vacancies Confined in Ultrathin Indium Oxide Porous Sheets for Promoted Visible-Light Water Splitting. *J. Am. Chem. Soc.* **2014**, *136*, 6826−6829.
(42) Bang, S.; Lee, S.; Ko, Y.; Park, J.; Shin, S.; Seo, H.; Jeon, H. Photocurrent Detection of Chemically Tuned Hierarchical ZnO Nanostructures Grown on Seed Layers Formed by Atomic Layer Deposition. *Nanoscale Res. Lett.* **2012**, *7*, 290.
(43) Kim, Y. H.; Kim, D. G.; Maduwu, R. D.; Jin, H. C.; Moon, D. K.; Kim, J. H. Organic Electrolytes Doped ZnO Layer as the Electron Transport Layer for Bulk Heterojunction Polymer Solar Cells. *Sol. RRL* **2018**, *2*, 1800086.
(44) Jiang, L.; Li, J.; Huang, K.; Li, S.; Wang, Q.; Sun, Z.; Mei, T.; Wang, J.; Zhang, L.; Wang, N.; Wang, X. Low-Temperature and Solution-Processable Zinc Oxide Transistors for Transparent Electronics. *ACS Omega* **2017**, *2*, 8990−8996.
(45) Hu, Z.-A.; Xie, Y.-L.; Wang, Y.-X.; Xie, L.-J.; Fu, G.-R.; Jin, X.-Q.; Zhang, Z.-Y.; Yang, Y.-Y.; Wu, H.-Y. Synthesis of α-Cobalt Hydroxides with Different Intercalated Anions and Effects of Intercalated Anions on Their Morphology, Basal Plane Spacing, and Capacitive Property. *J. Phys. Chem. C* **2009**, *113*, 12502−12508.
(46) Liu, S.; Yang, H. B.; Hung, S. F.; Ding, J.; Cai, W.; Liu, L.; Gao, J.; Li, X.; Ren, X.; Kuang, Z.; Huang, Y.; Zhang, T.; Liu, B. Elucidating the Electrocatalytic CO_2 Reduction Reaction over a Model Single-Atom Nickel Catalyst. *Angew. Chem., Int. Ed.* **2020**, *59*, 798−803.
(47) Zhang, T.; Han, X.; Liu, H.; Biset-Peiró, M.; Zhang, X.; Tan, P.; Tang, P.; Yang, B.; Zheng, L.; Morante, J. R.; Arbiol, J. Quasi-Double-Star Nickel and Iron Active Sites for High-Efficiency Carbon Dioxide Electroreduction. *Energy Environ. Sci.* **2021**, *14*, 4847−4857.
(48) Ni, W.; Xue, Y.; Zang, X.; Li, C.; Wang, H.; Yang, Z.; Yan, Y.-M. Fluorine Doped Cagelike Carbon Electrocatalyst: An Insight into the Structure-Enhanced CO Selectivity for CO_2 Reduction at High Overpotential. *ACS Nano* **2020**, *14*, 2014−2023.

(49) Liu, Y.; Liu, Z.; Lu, N.; Preiss, E.; Poyraz, S.; Kim, M. J.; Zhang, X. Facile Synthesis of Polypyrrole Coated Copper Nanowires: A New Concept to Engineered Core−Shell Structures. *Chem. Commun.* **2012**, *48*, 2621−2623.
(50) Dunwell, M.; Luc, W.; Yan, Y.; Jiao, F.; Xu, B. Understanding Surface-Mediated Electrochemical Reactions: CO_2 Reduction and Beyond. *ACS Catal.* **2018**, *8*, 8121−8129.
(51) Zhao, C.; Wang, Y.; Li, Z.; Chen, W.; Xu, Q.; He, D.; Xi, D.; Zhang, Q.; Yuan, T.; Qu, Y.; Yang, J.; Zhou, F.; Yang, Z.; Wang, X.; Wang, J.; Luo, J.; Li, Y.; Duan, H.; Wu, Y.; Li, Y. Solid-Diffusion Synthesis of Single-Atom Catalysts Directly from Bulk Metal for Efficient CO_2 Reduction. *Joule* **2019**, *3*, 584−594.
(52) Li, C. W.; Kanan, M. W. CO_2 Reduction at Low Overpotential on Cu Electrodes Resulting from the Reduction of Thick Cu_2O Films. *J. Am. Chem. Soc.* **2012**, *134*, 7231−7234.
(53) Gu, J.; Hsu, C.-S.; Bai, L.; Chen, H. M.; Hu, X. Atomically Dispersed Fe^{3+} Sites Catalyze Efficient CO_2 Electroreduction to CO. *Science* **2019**, *364*, 1091−1094.
(54) Chen, K.; Cao, M.; Ni, G.; Chen, S.; Liao, H.; Zhu, L.; Li, H.; Fu, J.; Hu, J.; Cortés, E.; Liu, M. Nickel Polyphthalocyanine with Electronic Localization at the Nickel Site for Enhanced CO_2 Reduction Reaction. *Appl. Catal., B* **2022**, *306*, 121093.
(55) Zhu, L.; Lin, Y.; Liu, K.; Cortés, E.; Li, H.; Hu, J.; Yamaguchi, A.; Liu, X.; Miyauchi, M.; Fu, J.; Liu, M. Tuning the Intermediate Reaction Barriers by a CuPd Catalyst to Improve the Selectivity of CO_2 Electroreduction to C2 Products. *Chin. J. Catal.* **2021**, *42*, 1500−1508.
(56) Luo, W.; Zhang, Q.; Zhang, J.; Moioli, E.; Zhao, K.; Züttel, A. Electrochemical Reconstruction of ZnO for Selective Reduction of CO_2 to CO. *Appl. Catal., B* **2020**, *273*, 119060.

https://doi.org/10.1021/acsami.2c09129
ACS Appl. Mater. Interfaces 2022, 14, 32157−32165